Towards a realistic model for cavity-enhanced atomic frequency comb quantum memories

Taherizadegan, Shahrzad; Davidson, Jacob H.; Kumar, Sourabh; Oblak, Daniel; Simon, Christoph

DOI
10.1088/2058-9565/ad4f0d

Publication date
2024

Document Version
Final published version

Published in
Quantum Science and Technology

Towards a realistic model for cavity-enhanced atomic frequency comb quantum memories

IOP Publishing Quantum Sci. Technol. 9 (2024) 035049 https://doi.org/10.1088/2058-9565/ad4f0d

Quantum Science and Technology

OPEN ACCESS

RECEIVED
12 December 2023

REVISED
12 May 2024

ACCEPTED FOR PUBLICATION
22 May 2024

PUBLISHED
25 June 2024

PAPER

Towards a realistic model for cavity-enhanced atomic frequency comb quantum memories

Shahrzad Taherizadegan[1,*], Jacob H Davidson[2,3], Sourabh Kumar[1], Daniel Oblak[1] and Christoph Simon[1]

[1] Department of Physics & Astronomy, Institute for Quantum Science and Technology, University of Calgary, 2500 University Drive NW, Calgary, Alberta T2N 1N4, Canada
[2] QuTech and Kavli Institute of Nanoscience, Delft University of Technology, 2600 GA Delft, The Netherlands
[3] Present Address: National Institute of Standards and Technology (NIST), Boulder, Colorado 80305, United States of America.
[*] Author to whom any correspondence should be addressed.

E-mail: shahrzad.taheri@ucalgary.ca

Keywords: quantum networks, quantum communication, quantum memory, optics, quantum repeaters, Kramers–Kronig relations

Abstract

Atomic frequency comb (AFC) quantum memory is a favorable protocol in long distance quantum communication. Putting the AFC inside an asymmetric optical cavity enhances the storage efficiency but makes the measurement of the comb properties challenging. We develop a theoretical model for cavity-enhanced AFC quantum memory that includes the effects of dispersion, and show a close alignment of the model with our own experimental results. Providing semi-quantitative agreement for estimating the efficiency and a good description of how the efficiency changes as a function of detuning, it also captures certain qualitative features of the experimental reflectivity. For comparison, we show that a theoretical model without dispersion fails dramatically to predict the correct efficiencies. Our model is a step forward to accurately estimating the created comb properties, such as the optical depth inside the cavity, and so being able to make precise predictions of the performance of the prepared cavity-enhanced AFC quantum memory.

1. Introduction

Optical quantum memory with the ability to store and recall on-demand quantum states of light with high efficiency and fidelity [1–3] is one of the essential elements for long-distance quantum communication based on quantum repeaters [4, 5]. It also has several applications in linear-optical quantum computation, single-photon detection, quantum metrology, and tests of the foundations of quantum physics [6].

Atomic frequency comb (AFC) quantum memory [7, 8] is a promising candidate in quantum repeater applications because of the capability to simultaneously store and read out multiple temporal and spectral modes that could enhance the performance of the quantum repeater via faster entanglement generation [9–15]. Also, as opposed to other quantum memory protocols, with the AFC technique, the number of temporal modes stored in a sample is independent of the optical depth of the storage medium [7].

To implement AFC quantum memory, rare-earth-ion doped crystals are particularly suitable due to the long coherence times of their optical 4f–4f transitions at cryogenic temperature [16, 17]. Long optical storage time has been demonstrated in rare-earth ion-doped crystal-based AFC quantum memory by using dynamical decoupling techniques to increase the spin coherence time [18–20].

The efficiency of the AFC quantum memory was improved by enhancing the preparation procedure of the AFC. These include optimization of the comb shape in Tm:YAG crystal [21] where some improvement in the efficiency has been demonstrated compared to the initial preparation procedure of the AFC [8, 22], and creation of high resolution (large finesse) AFCs by optimizing the pulse sequence which has been demonstrated in Er:YSO using hyperfine levels [23] leading to improvement in the AFC quantum memory efficiency.

To achieve high efficiency in quantum memories, a large optical depth in the storage material is typically needed. However, in practice, simultaneously achieving high optical depth and long coherence times is difficult [24]. This trade-off is exemplified by the observation that the coherence time is usually inversely dependent on the doping concentration. So, to have high coherence times, it is preferable to work with lower optical depth (OD) rare-earth doped crystals. To overcome this limitation, it was proposed to incorporate the storage medium in an asymmetric optical cavity. By applying the impedance matching condition, unit efficiency can, in principle, be obtained with an effective OD of only one [25, 26]. In this situation, the memory efficiency is only limited by intrinsic atomic dephasing.

So far, several experiments have been carried out based on the impedance matching proposal [25, 26] using the AFC technique [27–32]. To date, the best efficiencies obtained are 62% [32] for the storage time of 2 μs, 56% [27] for the storage time of 1.1 μs and 53% [28] for the storage time of 2 μs. Based on the experimental results, between 12–20 fold enhancement in the storage efficiency has been obtained by putting the AFC memory in an impedance-matched optical cavity compared to the no cavity case. However, it has been experimentally difficult to measure the AFC properties, e.g. OD within the impedance-matched cavity [27, 30, 31] because it is no longer straightforward to determine it from the measured frequency-dependent transmission using Beers law, as is the case for a crystal without a cavity. The fact that no detailed general theoretical model for cavity-enhanced AFC quantum memory exists, makes it difficult to compare experiments to theory, and hence also to infer the system parameters from experiments. The original proposal [25, 26] assumed a memory bandwidth significantly smaller than the cavity bandwidth to satisfy the resonance condition, and so did not discuss the combs that are created at frequencies detuned from the cavity resonance. Also, the background absorption due to imperfect optical pumping used to create the comb shape was ignored. Although, authors in [33, 34] have investigated the role of dispersion in AFC as a protocol closely associated to the slow-light-based storage protocols, so far there has not been a theoretical model for cavity-enhanced AFC quantum memory that includes the dispersion originating from the absorption engineering of ions to create the comb inside the cavity.

Here we develop a more general model that addresses all of these points. We extend the impedance-matched model beyond the resonance condition by including the round-trip phase shifts of light as travelling inside the cavity in the initial proposal [25] making it valid for any AFC bandwidth with a background absorption, and created at any detuning with respect to the cavity resonance. We show that, including dispersion, our developed model closely aligns with our own experimental results, and in particular enables prediction of the experimental memory efficiency at any detuning with respect to the cavity resonance. The paper is organized as follows: In sections 2 and 3 the theoretical model and the experiment performed are discussed. In section 4 the method to predict the cavity-enhanced AFC quantum memory reflectivity and efficiency is explained. Furthermore, we show results from the theory and compare them to the experimental data. In section 5 we elaborate on a comparison to a theoretical model without dispersion, and the conclusion and outlook are given in section 6.

2. Theoretical model for cavity-enhanced AFC quantum memory

An AFC quantum memory consists of an ensemble of inhomogeneously broadened atoms engineered as periodically comb-like peaks in frequency domain (see figure 1), which is realized through frequency-selective optical pumping of atoms from the ground state to a metastable state, e.g. a hyperfine state. A resonant input pulse with the bandwidth that matches the comb bandwidth is collectively absorbed. After absorption of the light, the collective excitation initially starts dephasing; however, after a time $t = 1/\Delta$, (Δ is the spectral distance between the peaks in Hz), due to the periodic structure of the comb, the excitation will be in phase again which leads to the echo pulse [7].

We consider an AFC quantum memory with OD contrast d_c and a background absorption OD d_0 inside a general asymmetric cavity with mirror reflectivities R_1 and R_2 where $R_1 < R_2 \approx 1$ (see figure 1) and apply the 'sum over all round-trips' approach of a Fabry–Perot cavity. We include absorption factors both for the frequency comb and the background due to additional background absorption to obtain the reflected intensity from the cavity. Furthermore, to extend the impedance-matched proposal for off-resonant combs with an arbitrary bandwidth, we include the phases associated with each path in the sum over all round trips (compared to the on resonance equation (11) in [25]). The reflected amplitude ($E_{\text{out}}/E_{\text{in}}$) from the cavity [35, 36] can be written as

$$\frac{E_{\text{out}}}{E_{\text{in}}} = \frac{-\sqrt{R_1} + \sqrt{R_2}\mathrm{e}^{-\mathrm{d}(\nu)}\mathrm{e}^{-\mathrm{i}\Phi(\nu)}}{1 - \sqrt{R_1 R_2}\mathrm{e}^{-\mathrm{d}(\nu)}\mathrm{e}^{-\mathrm{i}\Phi(\nu)}} \quad , \tag{1}$$

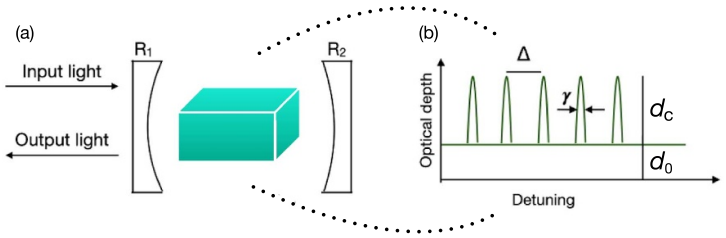

Figure 1. (a) Crystal inside a general asymmetric cavity with mirror reflectivities R_1 and R_2 where $R_1 < R_2 \approx 1$. (b) The natural inhomogeneously broadened absorption profile of the medium (Tm:YAG in this paper) is shaped into a comb structure where the peaks are separated by Δ and have a width (FWHM) of γ as shown on the right. The finesse of the comb is defined as $F = \frac{\Delta}{\gamma}$. Note FWHM peak width γ is related to the peak width $\tilde{\gamma}$ through $\gamma = \sqrt{8\ln 2}\,\tilde{\gamma}$. Due to the comb structure, there will be a coherent re-emission after a time $\frac{1}{\Delta}$.

where L is the length of the crystal, $\mathrm{d}(\nu) = \alpha(\nu) L$ is the OD, and $\alpha(\nu)$ is the frequency-dependent absorption coefficient. In addition, the total round-trip phase is $\Phi = 2KL$, where $K = 2\pi \frac{n(\nu)}{\lambda}$ is the wavenumber, and $n(\nu)$ is the real refractive index of the matter inside the cavity. $\Phi(\nu)$ can be written as

$$\Phi(\nu) = 4\pi \frac{n(\nu)\,\nu L}{c} \quad , \tag{2}$$

where c is the speed of light in the vacuum.

Equation (1) for the reflected amplitude can be interpreted as the response function of the cavity. We will refer to both terms interchangeably. Since E_{out} contains terms which depend on the OD and the phases associated with each path in the sum over all round-trips, the reflectivity of the cavity will become frequency dependent over the comb bandwidth. Equation (1) is a general version of equation (11) in [25] and can be applied to both on-resonance and off-resonance conditions. In section 4, we use equation (1) to simulate the reflectivity of the cavity and compare it with the experimental data.

We assume an AFC with an engineered OD $\mathrm{d}(\nu)$ of a series of Gaussian peaks with identical amplitudes (d_c), spacing (Δ), width ($\tilde{\gamma}$), and a constant d_0 which is the OD associated with the background absorption. The AFC OD $\mathrm{d}(\nu)$ can be written as

$$\mathrm{d}(\nu) = \sum_{k=1}^{9} d_c\, e^{-\frac{(\nu - b_k)^2}{2\tilde{\gamma}^2}} + d_0 \quad , \tag{3}$$

where the number 9 in the summation is the number of created teeth in the experiment, b_k is the center of each Gaussian function (each AFC tooth) and $b_k - b_{k-1} = \Delta$ (see figure 1). The OD of the crystal defines the initial $\alpha(\nu)$, and optical pumping to define the comb reshapes the natural absorption profile. The resulting profile can be described using d_0 for residual unaffected absorption, and $\mathrm{d}(\nu)$ for the total absorption corresponding to the newly shaped comb features.

By including the dispersion originating from the atomic absorption in the model there is a frequency-dependent refractive index $n(\nu)$ in the phase Φ. The complex refractive index $\tilde{n}(\nu)$ can be written as $\tilde{n}(\nu) = n(\nu) + \mathrm{i}k(\nu)$. The real part of the complex refractive index $n(\nu)$ is responsible for the change in the phase of light (see equation (2)). The imaginary part of the complex refractive index $k(\nu)$ is related to the absorption coefficient as,

$$k(\nu) = \frac{\alpha(\nu)\, c}{4\pi\, \nu} \quad . \tag{4}$$

The real and imaginary parts of the complex refractive index $\tilde{n}(\nu)$ are connected through the Kramers–Kronig relations, through the real $\chi_r(\nu)$ and imaginary $\chi_i(\nu)$ parts of the susceptibility of a medium [37–41]

$$\chi_r(\nu) = \frac{2}{\pi}\mathcal{P}\int_0^{\infty} \frac{\nu'\chi_i(\nu')}{\nu'^2 - \nu^2}\mathrm{d}\nu' \quad ,$$

$$\chi_i(\nu) = \frac{2}{\pi}\mathcal{P}\int_0^{\infty} \frac{\nu\chi_r(\nu')}{\nu^2 - \nu'^2}\mathrm{d}\nu' \tag{5}$$

where $\mathcal{P}$ symbolizes the Cauchy principal value. Note that in these equations ν is the absolute frequency, whereas we show the detuning in most of the rest of the paper. Thus, a frequency-dependent absorption

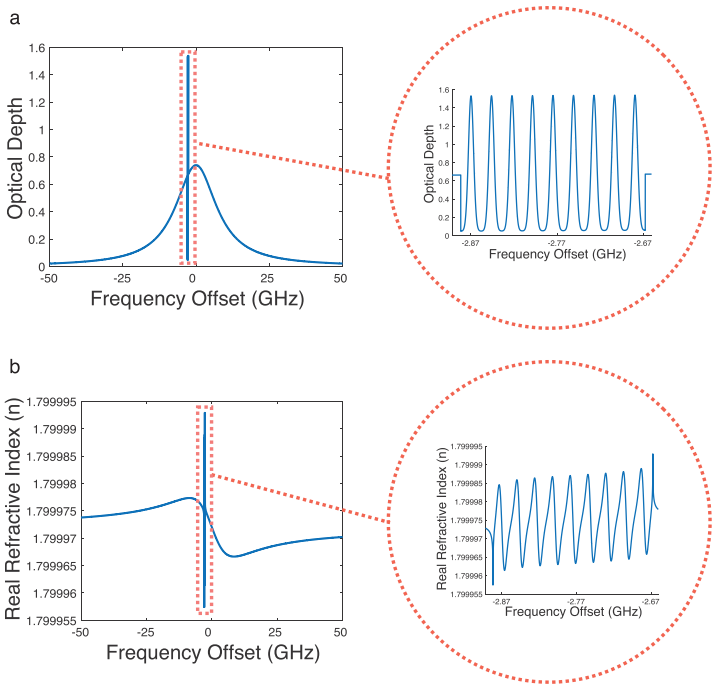

Figure 2. (a) The natural inhomogeneously broadened optical depth of Tm:YAG crystal with the comb-shape engineered optical depth for the comb at −2.7720 GHz detuning with respect to the center of the inhomogeneous broadening embedded into that. (**Inset**) The created comb-shaped optical depth over the comb bandwidth. (b) The calculated real refractive index $n(\nu)$ over the entire frequency range for the optical depth shown in (a). (**Inset**) $n(\nu)$ over the comb width.

coefficient results in a frequency-dependent $k(\nu)$ and it affects the real refractive index $n(\nu)$. Using the Kramers–Kronig relations (equation (5)) we can write the the real part of the complex refractive index $n(\nu)$ as

$$n(\nu) = n + \frac{2}{\pi}\mathcal{P}\int_0^\infty \frac{\nu' k(\nu')}{\nu'^2 - \nu^2} \mathrm{d}\nu' \ , \tag{6}$$

n is the constant real refractive index of the host crystal (YAG in this paper) [42, 43]. Putting the obtained $n(\nu)$ for the comb in equation (2), the change in phase of light Φ is calculated and one can write the equation for Φ as

$$\Phi(\nu) = 4\pi \frac{\nu L}{c}\left(n + \frac{2}{\pi}\mathcal{P}\int_0^\infty \frac{\nu' k(\nu')}{\nu'^2 - \nu^2} \mathrm{d}\nu'\right) \tag{7}$$

Note that to calculate the real refractive index $n(\nu)$ at each frequency the absorption coefficient must be defined over the entire frequency range. Figure 2(a) shows an example of the employed OD for a comb created close to the cavity resonance. Employing such an absorption coefficient allows us to calculate the real refractive index $n(\nu)$ over the comb. Figure 2(b) shows the calculated real refractive index $n(\nu)$ for the comb shown in figure 2(a). Using equation (7) for Φ, one can calculate the reflectivity of the cavity-enhanced AFC quantum memory as a function of frequency which will be done in section 4.

3. Experiment

We have performed our experiments in a 0.1% thulium-doped $Y_3Al_5O_{12}$ (Tm:YAG) crystal cavity, the same as used in [31]. The optical transition wavelength of Tm^{3+} is well suited for free-space quantum communication, making it attractive for ground-to-satellite communication, for example, for Canada's QEYSSat satellite mission [44–47]. Furthermore, its wavelength is compatible with quantum memories based on rubidium gas, allowing the possibility of designing hybrid platforms [48, 49]. Tm:YAG has wide inhomogeneous broadening (∼20 GHz) and narrow homogeneous linewidth (∼10 KHz) [50], in principle, permitting broadband, multimode, and long-lived quantum memories.

Our crystal is approximately 4 mm long and the AFCs are generated at a cryogenic temperature of 1.5 K. The two ends of the crystal surface are reflection coated with approximate reflectivities $R_1 = 40\%$ on the

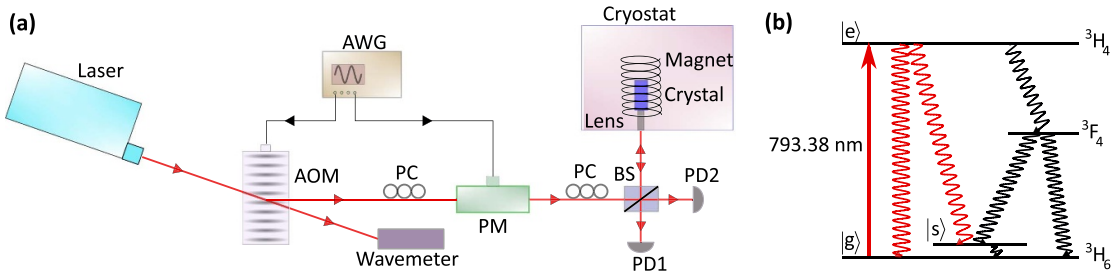

Figure 3. (a) Schematic of the experimental setup. A tunable external cavity diode laser serves as the light source. The first order of the acousto-optic modulator (AOM) goes through a polarization controller (PC) before passing an electro-optic phase modulator (PM). An arbitrary waveform generator (AWG) sends electrical signals to drive the AOM and the PM and control the experimental sequence. The 50/50 beamsplitter ensures that the same optical fiber transmits light to the crystal and collects the reflected light. The photodetector PD1 detects the back-reflected light from the crystal cavity whereas detector PD2 monitors the input laser light intensity. The sample is kept inside an adiabatic demagnetization refrigerator (ADR) and another superconducting magnet placed inside the cryostat applies a DC magnetic field to the crystal sample. (b) Energy level diagram of Tm^{3+} ion. For optical pumping, the laser is tuned to the $|g\rangle \rightarrow |e\rangle$ transition. Under the application of an external magnetic field, the ground state splits into Zeeman levels $|g\rangle$ and $|s\rangle$. The latter serves as the auxiliary level for the formation of the AFC. The echo after the storage time is emitted at the $|g\rangle \rightarrow |e\rangle$ transition frequency.

front end and $R_2 = 99\%$ on the back end [31] to satisfy the impedance matching condition. As a result, the created asymmetric optical cavity has a finesse close to 7 and free spectral range close to 20 GHz.

Figure 3(a) shows the experimental setup. Light near 793 nm from an external cavity diode laser (ECDL) passes through an acousto-optic modulator (AOM) driven at 400 MHz. While the zeroth order of the AOM is monitored on a wavemeter to measure the wavelength of the laser, the first diffracted order is directed to the crystal in the cryostat after passing through a phase modulator (PM) and a 50/50 beamsplitter. The energy level structure of Tm^{3+} ions is shown in figure 3(b). Under the application of an external magnetic field, the ground state $^3H_6$ splits into the Zeeman levels $|g\rangle$ and $|s\rangle$. The phase modulator is used to carve out the combs by selectively pumping ions in the frequency domain from the ground state $|g\rangle$ to the spin state $|s\rangle$ [31], mediated by the excited state $|e\rangle$. The 50/50 beamsplitter is employed to be able to send and receive photons by back-reflection from the cavity using the same optical fiber. The optical fiber is terminated in a ferrule, which is placed in front of a gradient index (GRIN) lens. Both the ferrule and lens are inserted in a tight-fitting 50 mm long capillary, which is fixed at one end to the crystal mount and at the other to a xyz nano-positioning stage. In this way, movement of the nanopositioner will change the angle of the capillary, and, thus, the enclosed fibre and GRIN lens, to the crystal surface allowing the input mode to be aligned to the cavity mode.

AFC combs are created at varying frequencies across the cavity spectrum by tuning the ECDL frequency. For measurements of the cavity reflection spectrum, the ECDL frequency can also be continuously swept across nearly 50 GHz. The strength of the external magnetic field controls the Zeeman splitting between the spin levels $|g\rangle$ and $|s\rangle$. We choose a magnetic field value close to 500 Gauss such that during the optical pumping in the AFC preparation, the atoms from the AFC troughs are almost all moved to the AFC peaks, increasing their OD nearly by a factor of two [31]. This efficient AFC preparation ensures that almost all the atoms participate in the absorption and re-emission process. An arbitrary waveform generator (AWG) drives the AOM and the PM to create the experimental sequence for optical pumping and input pulse generation. After 50 ms optical pumping and 5 ms wait time, we send in narrow-band input pulses generated by the AOM. The back-reflected light, after passing through the beamsplitter, is collected on one of the photodetectors (PD1 in figure 3(a)). We tune the laser to different wavelengths and record the AFC scans at each wavelength. The scans are obtained with the help of a phase modulator, which generates a linear chirp spanning the whole AFC width. The frequency spanned is 200 MHz in 100 μs. The photodetector PD1 detects the chirped light after interacting with the AFC profiles and the AFC scans are obtained on an oscilloscope connected to PD1. We repeat the experimental sequence 100 times with a 200 ms interval between each repetition to reduce the experimental noise and generate a steady AFC. We take the average of these 100 scans on the oscilloscope to obtain the effective AFC trace. After the AFC trace is collected at a particular wavelength, we send an input pulse centered at that wavelength. We observe the unabsorbed part of the pulse and the echoes emitted on the oscilloscope connected to PD1. Similar to the AFC scans, we repeat the experimental sequence 100 times and take the average to obtain the effective traces for the pulses and the echoes. To obtain the input electric field (E_{in}) in equation (1), we go to an off-resonant frequency, greater than 200 GHz away from the center of the inhomogeneous broadening. Since almost no atoms interact with the incident light at this wavelength, the AFC trace is close to a flat line. Also, virtually no part of the incident

pulse is absorbed at this wavelength and no echoes are emitted. The unabsorbed part of the incident pulse is now taken as the input pulse for calculating the memory efficiencies. We monitor the fluctuations in the input power of the laser as we tune its wavelength by connecting the free port of the beamsplitter to another photodetector (PD2) as shown in figure 3(a). We calculate the experimental efficiencies by dividing the area of the first echo at each wavelength by the area of the input pulse. The maximum experimental efficiency is obtained for the comb close to the cavity resonance frequency and at the detuning of −2.7720 GHz from the resonance frequency of the atoms (all the detunings in the present manuscript are with respect to the center frequency of the inhomogeneously broadened atomic transition, unless otherwise mentioned).

Using the theory discussed in section 2 and this experimental setup we are able to extract some relevant features of our memories and verify the performance of our new model in the following section.

4. Results and discussion

In this section, we show and analyze the experimental results. First, equation (1) is fitted with the experimental data for the reflectivity of the crystal cavity with no comb carved into it and the values of the crystal cavity properties are obtained as the fitting parameters in section 4.1. Note that equation (1) is for the reflected amplitude and not the reflected power ($|\text{reflected amplitude}|^2 = \text{reflected power}$). Next, the crystal cavity with a spectral-shaped AFC is considered. By fitting the model to the measurement results for the reflectivity and using the obtained fitting parameters for the crystal cavity properties from the previous step, the shape and OD of the created combs are extracted as shown in section 4.2. The fitting scripts are all coded in Matlab [51], and the curve fitting and optimization toolboxes are applied. Finally, the obtained comb properties from the fitting are used to predict the efficiencies of the created cavity AFC quantum memories at various frequency offsets across the cavity profile in section 4.3, and the predicted memory efficiencies are compared to the experimental results.

4.1. Cavity reflectivity without comb

The reflected power at different frequencies for the crystal cavity with no AFC carved into it can be obtained using equation (1). The values of the crystal cavity properties are obtained as the fitting parameters from fitting equation (1) in the model with the experimental normalized reflected power for the Tm:YAG crystal cavity with no comb engineered into it as measured in [31]. The real refractive index $n(\nu)$ in equation (2) is frequency dependent and can be obtained using equation (6) (section 2). The inhomogeneously broadened absorption spectrum of Tm in YAG is a Lorentzian function centered at $\nu_0 = 377\,868$ GHz, with a FWHM of $\Gamma_{\text{in}} = 17$ GHz [52]. Figure 4 shows the data for the reflectivity of the cavity at different frequencies and the fitted curve to the data. We see three cavity resonances in the figure. Near impedance-matching occurs at the frequency offset of −3.19 GHz. It should be noted that the impedance-matched point is close to the perfect impedance-matching: theoretically 100% of the input light should be absorbed at the impedance-matched frequency (zero reflection); however, the experimental value got close to 95% absorption. The obtained impedance-matched frequency for the fitted curve is in good agreement with the experimental value of -3.4 ± 0.5 GHz where the uncertainty in the measured value comes from our optical wavemeter smallest significant digit. The maximum value of the Lorentzian function of the absorption spectrum is also set as a fitting parameter. This takes into account possible variations in crystal growth and sections of the boule from which our sample was cut. Although the experimental cavity reflection data (figure 4) is measured through a 50/50 beamsplitter, the measured maximum reflectivity value of slightly more than 0.5 in figure 4 implies the employed beamsplitter was not exactly a 50/50 one. To account for that there is a factor of s as a fitting parameter so that (reflected power / s) is fitted to the experiment, with $s = 2$ corresponding to an ideal 50/50 beamsplitter. The obtained values for the crystal cavity parameters are shown in table 1. Also, the obtained peak absorption coefficient ($\alpha_{\text{peak}} = 1.70\ \text{cm}^{-1}$) is in good agreement with the measured value of between 1.9 cm^{-1} to 2.3 cm^{-1} [50, 52].

In the next step the obtained fitting parameters for the crystal cavity properties are used to analyze the experimental reflectivity of the cavity-enhanced AFC quantum memory.

4.2. Cavity reflectivity with comb

In this section the experimental data for the reflected power of the cavity-enhanced AFC quantum memories created at different detunings are analyzed to extract the combs' features. As stated in the section 2 it is assumed the AFC is a series of Gaussian functions with the same amplitude (d_c), spacing (Δ), width ($\tilde{\gamma}$), and with a constant background absorption d_0 (see equation (3)). We use equation (7) to calculate the phase Φ. Then equation (1) is fitted to the experimental data for the reflected power of each of the memories at different wavelengths and the comb parameters d_c, Δ, $\tilde{\gamma}$, and d_0 are extracted as the fitting parameters. The fitted curves to the experimental reflected power using the model equations are shown in figure 5 and the

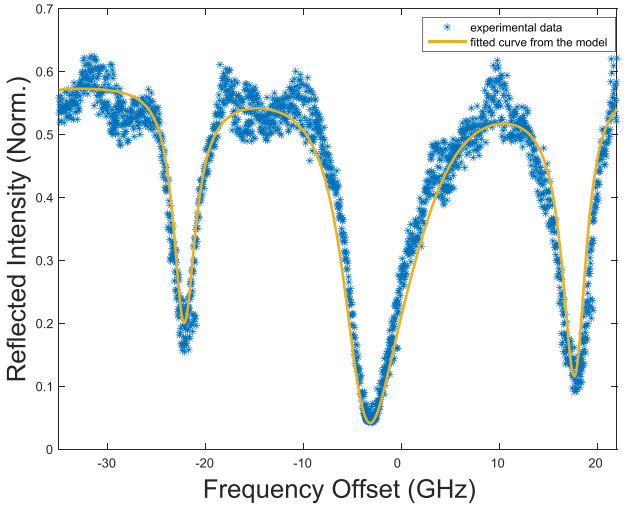

Figure 4. Experimental cavity reflectivity and the fitted curve from the model.

Table 1. Obtained parameters for crystal cavity properties from cavity reflectivity without comb (see figure 4).

Crystal cavity properties		
Peak absorption coefficient	α_{peak} (cm^{-1})	1.70
Front mirror reflection	$r_1 = \sqrt{R_1}$	0.6927
Back mirror reflection	$r_2 = \sqrt{R_2}$	0.9999
Constant refractive index	n	1.799 972
Cavity/crystal length	L (cm)	0.4350
Beam-splitter ratio	s	1.7142

Table 2. Obtained comb parameters for cavity-enhanced AFC quantum memories created at different detunings across the cavity profile (see figure 5).

Comb properties	Comb a	Comb b	Comb c
d_c	1.5260	1.4867	1.4261
Δ (MHz)	23.4598	23.8160	24.3382
$\tilde{\gamma}$ (MHz)	3.6063	2.9755	3.4462
d_0	0.2008	0.0526	0.0254

extracted fitting parameters are shown in table 2 for three AFCs created at three critical regions across the cavity features (see figure 5(d)). The first one is the AFC created far from the cavity resonance at the detuning of 2.2765 GHz with respect to the resonance frequency of the atoms (see figure 5(a)). The second one is close to the impedance-matched frequency at the detuning of −2.7720 GHz (see figure 5(b)). The third comb is in an intermediate regime, and on the other side of the cavity resonance at the detuning of −3.8675 GHz (see figure 5(c)).

Figures 5(a) and (c) show there is an asymmetry (skewness) at the bottom of the experimental data for the reflectivity of the combs created at 2.2765 GHz and −3.8675 GHz, which is captured in the fitted curves obtained from the model. In figure 5 for the shown combs, the skewness at the bottom of the reflected power data changes direction as one moves from one side to the other side of the cavity resonance, which is also true for all the other combs that are not shown, and is captured by the model. Also, for the comb created at −3.8675 GHz detuning (see figure 5(c)) there is an skewness around its lowest point at the bottom of the experimental data for all of the teeth in the comb captured to some extent in the model (for most of the teeth in the comb). Moreover, note the shapes at the top of the comb created close to the impedance-matched point at −2.7720 GHz frequency offset, and the fact that the maximum of the experimental reflectivity is lower as compared to the other two combs. As one can see in figure 5(b), relatively similar features are obtained by the model.

Discussing the obtained fitting parameters for the comb properties in the model, the spacing (Δ) between the teeth, which is related to the storage time of the AFC quantum memory, is very similar amongst

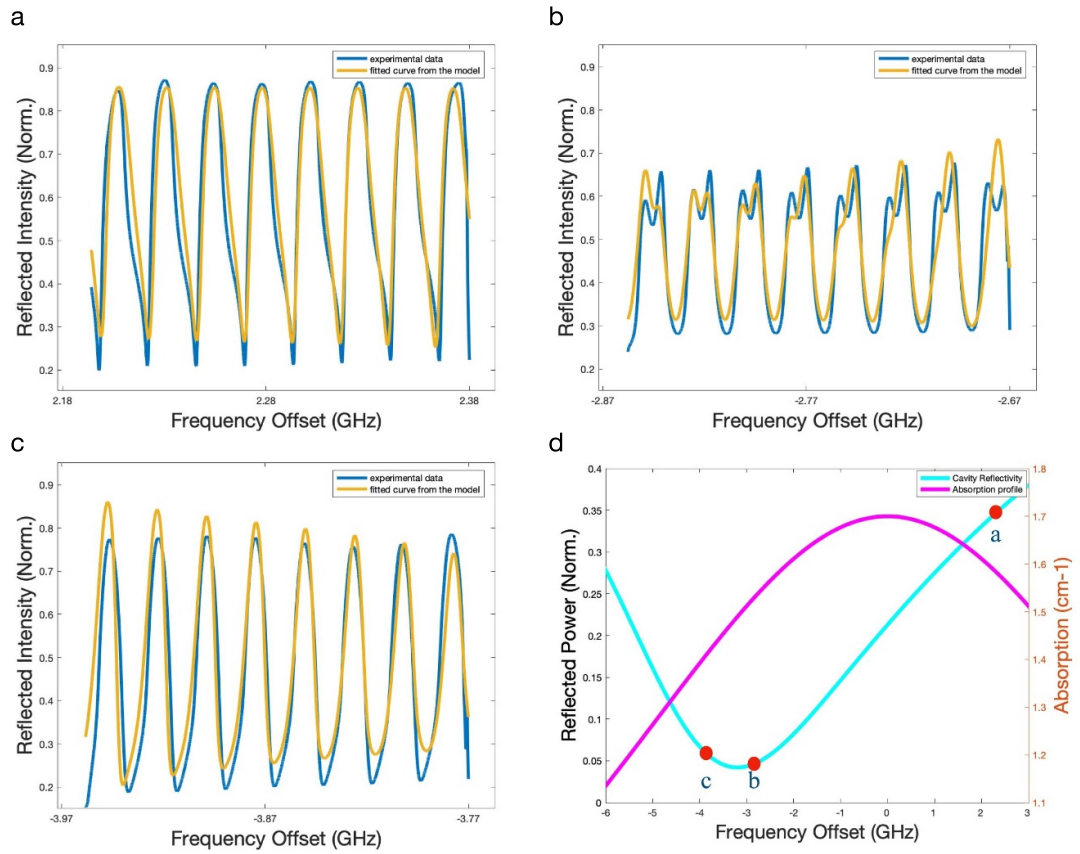

Figure 5. Experimental cavity-enhanced AFC quantum memory reflectivity and the fitted curves for three combs created at three critical regions across the cavity features. (a) shows a comb far from the impedance-matched frequency (at the detuning of 2.2765 GHz). (b) shows a comb close to the impedance-matched frequency (at the detuning of −2.7720 GHz). (c) shows a comb in an intermediate regime (at the detuning of −3.8675 GHz). (d) The inhomogeneously broadened absorption spectrum of (Tm:YAG) crystal and the reflectivity of the (Tm:YAG) crystal cavity over a smaller range (the range of the created combs). The locations of the above combs are labeled a, b, and c corresponding to the combs in subfigures (a)–(c).

the created AFCs as expected, and approximately the same as the model. Considering the storage time of 42 ns for the memories, one can obtain $\Delta = 23.81$ MHz, which is in good agreement with the extracted Δ values in table 2. Thus, the challenges to understand the comb features are mainly focused on achieving the true values for the atomic absorption depth and the width of the related combs. The obtained value of $\tilde{\gamma}$ in the model for each comb shown in figure 5 does not change a lot within different combs resulting in nearly the same values for the finesse of different combs as expected from the experiment. Considering the pumping procedure (section 3) and the inhomogeneous broadening in the absorption spectrum of Tm:YAG crystal, we expect somewhat lower d_c values compared to the ones obtained from the model. This leads to a difference between the theoretical and experimental efficiency which is discussed in the next section.

4.3. Memory efficiency

We now calculate the efficiencies of the created cavity-enhanced AFC quantum memories numerically taking the following steps. First, we take the Fourier transform (FT) of the input pulse sent for storage to the memory. Then by multiplying the input pulse in the frequency domain by the response function of the cavity (which contains the phase information), the output from the cavity AFC quantum memory is obtained in the frequency domain. Finally, the numerical inverse FT results in the output in the time domain. Calculating the square of the absolute value of the output to obtain the output intensity and then plotting the output intensity with respect to time one can obtain the cavity-enhanced AFC quantum memory efficiency by calculating the area under the first echo, i.e. the pulse that occurs after the storage time of the memory, and dividing it by the integrated input intensity. The obtained value is the calculated numerical efficiency of the cavity-enhanced AFC quantum memory. The numerical calculation is performed by coding in Matlab and using the Fast FT (FFT) algorithm.

Figure 6 shows the obtained output pulses with respect to time from the model for a cavity-enhanced AFC quantum memory created near the impedance-matched frequency. In the obtained output we see

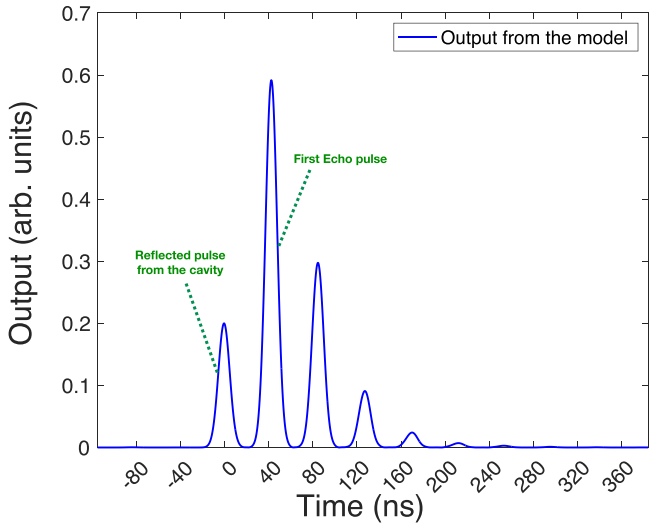

Figure 6. The output pulses obtained theoretically for a comb close to the impedance-matched frequency. Memory storage time of 42 ns is visible which is the difference between the occurrence time of the reflected part of the input pulse (not being absorbed and stored) and the first recalled (echo) pulse.

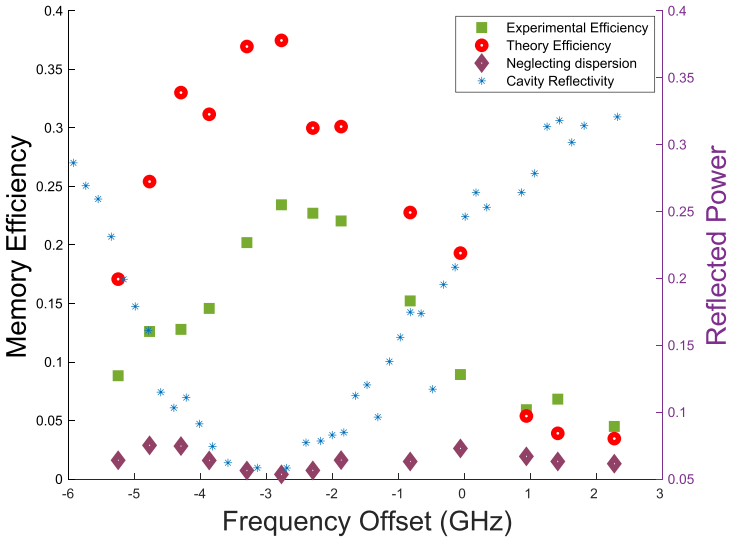

Figure 7. The measured experimental efficiency for the created combs and the theoretical efficiency obtained from the model. The blue points show a zoomed-in view of the crystal cavity reflectivity (figure 4) over the created combs' frequency range. Memory efficiencies neglecting the dispersion effect are shown for comparison (see text for more details).

several pulses where the first one is part of the input pulse reflected from the cavity, and the other remaining pulses are the echo pulses in a decreasing order.

The calculated efficiencies for all the combs created at different detunings across the cavity features are shown in figure 7 along with the measured experimental memory efficiencies. Based on the experimental data the maximum echo emission (efficiency) occurs for the AFC created close to the impedance-matched frequency. The obtained efficiency trend in the model is the same as the experiment, with the maximum efficiency for the comb created near the impedance-matched frequency.

The model still does not capture all features of the experimental reflectivity. For example, there is an asymmetry over the comb bandwidth in the fitted curve in figure 5(c), which is not exactly the same as the experiment. Also, for the comb created close to the impedance-matched point (figure 5(b)) we do not perfectly capture the features at the top of the experimental curve. Indeed, for different combs, these features appear differently. This leads to an inaccurate estimation of the combs' features and likely to an overestimation of the calculated memory efficiencies. These facts suggest that although the skewness in the

data may not seem that important at first look, it is important for being able to predict the combs' features precisely, and, so, to predict efficiencies close to the experimental values.

5. Comparison to a theoretical model without dispersion

It is worth investigating the effect of neglecting dispersion due to the atomic absorption, leading to a constant real refractive index n in equation (2) for the YAG crystal [42, 43]. One can do the process of fitting equation (1) to the experimental data for the cavity reflectivity without and with comb the same as sections 4.1 and 4.2 and extract the comb parameters as the fitting parameters. Doing so the skewness at the bottom of the experimental reflected power data for the combs created far from the impedance-matched frequency (figure 5(a)), and in an intermediate regime (figure 5(c)), and also the shapes at the top of the comb created close to the impedance-matched point (figure 5(b)) are not captured in the fitted curves.

Talking about the obtained fitting parameters, although for each comb the obtained values of Δ, and d_0 remain relatively the same as before and there is a small change in the obtained value of $\tilde{\gamma}$, considering the pumping procedure (section 3) there is a noticeable misestimation in the obtained d_c values of the created combs. Our model lets us obtain more reasonable d_c values for the created combs.

Employing the same steps as section 4.3, we can calculate the efficiencies of the created AFCs at different detunings across the cavity profile. Figure 7 shows that the calculated efficiency for all the created combs is lower than the experimental results. Far from the cavity resonance there is only slight disagreement between the theoretical and experimental efficiencies, but as one gets closer to the cavity resonance the disagreement becomes much more prominent. This suggests that dispersion becomes more important for the combs created closer to the impedance-matched frequency (cavity resonance).

Note that the underestimation of the efficiency in the absence of dispersion is not purely due to the misestimation of d_c. Using the refractive index (n) as a fitting parameter, it is possible to obtain reasonable values for d_c even in the absence of dispersion, but the predicted efficiencies are still much too low. The underestimation of the efficiency is also due to the violation of causality in the absence of dispersion, which leads to an unphysical echo occurring before the input pulse associated with a reduction of the physical echos.

6. Conclusion and outlook

In summary, we have developed a model for cavity-enhanced AFC quantum memory, which helps to address the challenges of the measurement of comb properties inside the cavity. Employing the experimental cavity reflectivity, our model allows us to estimate the comb properties and the efficiency of the cavity-enhanced AFC quantum memory with a background absorption and arbitrary bandwidth created at any frequency offset with respect to the cavity resonance. Using the model, one obtains realistic values for the OD, as well as the correct trend for the efficiencies (they are maximum near resonance). Furthermore, the predicted values are in semi-quantitative agreement with the experimental ones. For comparison, we have also shown that a model without including dispersion completely fails to predict the memory efficiencies. Our results confirm the important role of dispersion effects in successfully modeling cavity-enhanced AFC quantum memories.

The model still does not capture all the features, which may be related to the fact that predicted efficiencies are somewhat higher than those achieved in experiments. This discrepancy is likely related to a number of points. First, the shape of the individual created teeth is not a perfect match to that of the model; they are closer to a rectangular shape rather than the assumed Gaussian shape. Second, residual reflectivity from the lenses causes some additional modulation on the transmitted intensity—due to a cavity being formed between the lens and the crystal—which affects the obtained parameters for the cavity. Third, averaging the experimental runs for each output trace can influence the experimental efficiency if some of the contributing runs featured lower efficiencies, e.g. from occasional laser instability.

Going forward, to upgrade AFC memory from predetermined storage time to on-demand readout, one can transfer the coherent excitation to a long-lived ground state spin coherence using optical control pulses which produce noise in the system [7, 10, 53–56]. Employing the Stark effect, it is possible to have an on-demand AFC quantum memory without the need for applying optical pulses and as a result being noise free [57].

Recently, a chip-integrated AFC quantum memory has been demonstrated using a thin-film lithium niobate waveguide doped with thulium (Tm^{3+}) rare-earth ions. Thin-film lithium niobate offers a more compact device structure compared to bulk material and is compatible with wafer-scale fabrication [58]. It would be interesting to adapt our theoretical model to a cavity with a waveguide crystal instead of a bulk crystal. Considering the new fabrication techniques for the waveguides and photonic materials being

available [59], compared to the older, lossy diffusion waveguides [60], an integrated cavity platform should be feasible experimentally. Advancement in nanofabricated rare-earth ion doped crystals platforms may enable arbitrary-scale arrays of quantum memories for multiplexed quantum repeaters [61].

This work is focused on the impedance-matched weak coupling regime. There are some works more focused on the strong coupling regime [62, 63] which have the potential advantage of faster and more efficient memory preparation by Purcell enhancing the spontaneous decay rate [61]. One potential future direction is to investigate the effect of going into strong light-matter coupling regime on the memory storage and retrieval process, where new phenomena may arise [64].

In sum, we anticipate that this work can further inform the next generation of cavity-enhanced quantum memories leading to more rapid progress towards their application in quantum networks.

Data availability statement

The data cannot be made publicly available upon publication because they are not available in a format that is sufficiently accessible or reusable by other researchers. The data that support the findings of this study are available upon reasonable request from the authors.

Acknowledgments

We wish to thank Roohollah Ghobadi, and Erhan Saglamyurek for useful discussions. This work was supported by the Alberta Major Innovation Fund (MIF), the High-Throughput Secure Networks (HTSN) Program of the National Research Council (NRC), Canada Foundation for Innovation (CFI), Alberta Innovates, and the Natural Sciences and Engineering Research Council (NSERC).

ORCID iDs

Shahrzad Taherizadegan https://orcid.org/0009-0007-2198-5063
Jacob H Davidson https://orcid.org/0009-0007-3064-6020
Daniel Oblak https://orcid.org/0000-0002-0277-3360

References

[1] Simon C *et al* 2010 Quantum memories *Eur. Phys. J.* D **58** 1
[2] Heshami K, England D G, Humphreys P C, Bustard P J, Acosta V M, Nunn J and Sussman B J 2016 Quantum memories: emerging applications and recent advances *J. Mod. Opt.* **63** 2005
[3] Ma L, Slattery O and Tang X 2020 Optical quantum memory and its applications in quantum communication systems *J. Res. Natl Inst. Stand. Technol.* **125** 125002
[4] Briegel H-J, Dür W, Cirac J I and Zoller P 1998 Quantum repeaters: the role of imperfect local operations in quantum communication *Phys. Rev. Lett.* **81** 5932
[5] Duan L-M, Lukin M D, Cirac J I and Zoller P 2001 Long-distance quantum communication with atomic ensembles and linear optics *Nature* **414** 413
[6] Bussieres F, Sangouard N, Afzelius M, De Riedmatten H, Simon C and Tittel W 2013 Prospective applications of optical quantum memories *J. Mod. Opt.* **60** 1519
[7] Afzelius M, Simon C, de Riedmatten H and Gisin N 2009 Multimode quantum memory based on atomic frequency combs *Phys. Rev.* A **79** 052329
[8] De Riedmatten H, Afzelius M, Staudt M U, Simon C and Gisin N 2008 A solid-state light–matter interface at the single-photon level *Nature* **456** 773
[9] Simon C, de Riedmatten H, Afzelius M, Sangouard N, Zbinden H and Gisin N 2007 Quantum repeaters with photon pair sources and multimode memories *Phys. Rev. Lett.* **98** 190503
[10] Gündoğan M, Mazzera M, Ledingham P M, Cristiani M and de Riedmatten H 2013 Coherent storage of temporally multimode light using a spin-wave atomic frequency comb memory *New J. Phys.* **15** 045012
[11] Lago-Rivera D, Grandi S, Rakonjac J V, Seri A and de Riedmatten H 2021 Telecom-heralded entanglement between multimode solid-state quantum memories *Nature* **594** 37
[12] Ortu A, Rakonjac J V, Holzäpfel A, Seri A, Grandi S, Mazzera M, de Riedmatten H and Afzelius M 2022 Multimode capacity of atomic-frequency comb quantum memories *Quantum Sci. Technol.* **7** 035024
[13] Jobez P, Timoney N, Laplane C, Etesse J, Ferrier A, Goldner P, Gisin N and Afzelius M 2016 Towards highly multimode optical quantum memory for quantum repeaters *Phys. Rev.* A **93** 032327
[14] Wei S-H *et al* 2024 Quantum storage of 1650 modes of single photons at telecom wavelength *npj Quantum Inf.* **10** 19
[15] Sinclair N *et al* 2014 Spectral multiplexing for scalable quantum photonics using an atomic frequency comb quantum memory and feed-forward control *Phys. Rev. Lett.* **113** 053603
[16] Thiel C W, Böttger T and Cone R 2011 Rare-earth-doped materials for applications in quantum information storage and signal processing *J. Lumin.* **131** 353
[17] Guo M, Liu S, Sun W, Ren M, Wang F and Zhong M 2023 Rare-earth quantum memories: the experimental status quo *Front. Phys.* **18** 21303

[18] Holzäpfel A, Etesse J, Kaczmarek K T, Tiranov A, Gisin N and Afzelius M 2020 Optical storage for 0.53 s in a solid-state atomic frequency comb memory using dynamical decoupling *New J. Phys.* **22** 063009
[19] Ma Y, Ma Y-Z, Zhou Z-Q, Li C-F and Guo G-C 2021 One-hour coherent optical storage in an atomic frequency comb memory *Nat. Commun.* **12** 2381
[20] Ortu A, Holzäpfel A, Etesse J and Afzelius M 2022 Storage of photonic time-bin qubits for up to 20 ms in a rare-earth doped crystal *npj Quantum Inf.* **8** 29
[21] Bonarota M, Ruggiero J, Le Gouët J-L and Chanelière T 2010 Efficiency optimization for atomic frequency comb storage *Phys. Rev.* A **81** 033803
[22] Chanelière T, Ruggiero J, Bonarota M, Afzelius M and Le Gouët J 2010 Efficient light storage in a crystal using an atomic frequency comb *New J. Phys.* **12** 023025
[23] Yasui S, Hiraishi M, Ishizawa A, Omi H, Inaba T, Xu X, Kaji R, Adachi S and Tawara T 2022 Creation of a high-resolution atomic frequency comb and optimization of the pulse sequence for high-efficiency quantum memory in $^{167}Er:Y_2SiO_5$ *Opt. Contin.* **1** 1896
[24] Tittel W, Afzelius M, Chaneliere T, Cone R L, Kröll S, Moiseev S A and Sellars M 2010 Photon-echo quantum memory in solid state systems *Laser Photon. Rev.* **4** 244
[25] Afzelius M and Simon C 2010 Impedance-matched cavity quantum memory *Phys. Rev.* A **82** 022310
[26] Moiseev S A, Andrianov S N and Gubaidullin F F 2010 Efficient multimode quantum memory based on photon echo in an optimal QED cavity *Phys. Rev.* A **82** 022311
[27] Sabooni M, Li Q, Kröll S and Rippe L 2013 Efficient quantum memory using a weakly absorbing sample *Phys. Rev. Lett.* **110** 133604
[28] Jobez P, Usmani I, Timoney N, Laplane C, Gisin N and Afzelius M 2014 Cavity-enhanced storage in an optical spin-wave memory *New J. Phys.* **16** 083005
[29] Sabooni M, Kometa S T, Thuresson A, Kröll S and Rippe L 2013 Cavity-enhanced storage-preparing for high-efficiency quantum memories *New J. Phys.* **15** 035025
[30] Akhmedzhanov R, Gushchin L, Kalachev A, Nizov N, Nizov V, Sobgayda D and Zelensky I 2016 Cavity-assisted atomic frequency comb memory in an isotopically pure $^{143}Nd^{3+}$: $YLiF_4$ crystal *Laser Phys. Lett.* **13** 115203
[31] Davidson J H, Lefebvre P, Zhang J, Oblak D and Tittel W 2020 Improved light-matter interaction for storage of quantum states of light in a thulium-doped crystal cavity *Phys. Rev.* A **101** 042333
[32] Duranti S, Wengerowsky S, Feldmann L, Seri A, Casabone B, and de Riedmatten H 2023 Efficient cavity-assisted storage of photonic qubits in a solid-state quantum memory (arXiv:2307.03509)
[33] Bonarota M, Le Gouët J, Moiseev S and Chaneliere T 2012 Atomic frequency comb storage as a slow-light effect *J. Phys. B: At. Mol. Opt. Phys.* **45** 124002
[34] Berman P and Le Gouët J-L 2021 Pulsed field transmission by atomic frequency combs and random spike media: the prominent role of dispersion *Phys. Rev.* A **103** 043723
[35] Pollnau M and Eichhorn M 2020 Spectral coherence, part I: passive-resonator linewidth, fundamental laser linewidth and schawlow-townes approximation *Prog. Quantum Electron.* **72** 100255
[36] Siegman A E 1986 *Lasers* (University Science Books)
[37] Kronig R d L 1926 On the theory of dispersion of x-rays *J. Opt. Soc. Am.* **12** 547
[38] Kramers H A 1927 La diffusion de la lumiere par les atomes *Atti Cong. Intern. Fisica (Trans. of Volta Centenary Congress) Como* vol 2 pp 545–57
[39] Toll J S 1956 Causality and the dispersion relation: logical foundations *Phys. Rev.* **104** 1760
[40] Lucarini V, Saarinen J J, Peiponen K-E and Vartiainen E M 2005 *Kramers-Kronig Relations in Optical Materials Research* vol 110 (Springer)
[41] Saleh B E A and Teich M C 1991 *Fundamentals of Photonics* (Wiley)
[42] Zelmon D E, Small D L and Page R 1998 Refractive-index measurements of undoped yttrium aluminum garnet from 0.4 to 5.0 μm *Appl. Opt.* **37** 4933
[43] Hrabovsky J, Kucera M, Palousová L, Bi L and Veis M 2021 Optical characterization of $Y_3Al_5O_{12}$ and $Lu_3Al_5O_{12}$ single crystals *Opt. Mater. Express* **11** 1218
[44] Lee Y S, Mohammadi K, Babcock L, Higgins B L, Podmore H and Jennewein T 2022 Robotized polarization characterization platform for free-space quantum communication optics *Rev. Sci. Instrum.* **93** 033101
[45] Jennewein T, Simon C, Fougeres A, Babin F, Asadi F K, Kuntz K B, Maisonneuve M, Moffat B, Mohammadi K, and Panneton D 2023 Qeyssat 2.0–white paper on satellite-based quantum communication missions in Canada (arXiv:2306.02481)
[46] Podmore H, D'Souza I, Cain J, Jennewein T, Higgins B, Lee Y, Koujelev A, Hudson D and McColgan A 2021 Qkd terminal for Canada's quantum encryption and science satellite (QEYSSat) *Proc. SPIE* **11852** 203–12
[47] Bourgoin J *et al* 2013 A comprehensive design and performance analysis of low earth orbit satellite quantum communication *New J. Phys.* **15** 023006
[48] Hosseini M, Sparkes B M, Campbell G, Lam P K and Buchler B C 2011 High efficiency coherent optical memory with warm rubidium vapour *Nat. Commun.* **2** 174
[49] Saglamyurek E, Hrushevskyi T, Rastogi A, Heshami K and LeBlanc L J 2018 Coherent storage and manipulation of broadband photons via dynamically controlled autler–townes splitting *Nat. Photon.* **12** 774
[50] Liu G and Jacquier B 2006 *Spectroscopic Properties of Rare Earths in Optical Materials* vol 83 (Springer)
[51] Lucarini V 2023 Tools for data analysis in optics, acoustics, signal processing (available at: www.mathworks.com/matlabcentral/fileexchange/8135-tools-for-data-analysis-in-optics-//acoustics-signal-processing)
[52] Veissier L, Thiel C W, Lutz T, Barclay P E, Tittel W and Cone R L 2016 Quadratic zeeman effect and spin-lattice relaxation of tm^{3+}:YAG at high magnetic fields *Phys. Rev.* B **94** 205133
[53] Afzelius M *et al* 2010 Demonstration of atomic frequency comb memory for light with spin-wave storage *Phys. Rev. Lett.* **104** 040503
[54] Amari A *et al* 2010 Towards an efficient atomic frequency comb quantum memory *J. Lumin.* **130** 1579
[55] Gündoğan M, Ledingham P M, Kutluer K, Mazzera M and de Riedmatten H 2015 Solid state spin-wave quantum memory for time-bin qubits *Phys. Rev. Lett.* **114** 230501
[56] Timoney N, Usmani I, Jobez P, Afzelius M and Gisin N 2013 Single-photon-level optical storage in a solid-state spin-wave memory *Phys. Rev.* A **88** 022324
[57] Horvath S P, Alqedra M K, Kinos A, Walther A, Dahlström J M, Kröll S and Rippe L 2021 Noise-free on-demand atomic frequency comb quantum memory *Phys. Rev. Res.* **3** 023099

[58] Dutta S, Zhao Y, Saha U, Farfurnik D, Goldschmidt E A and Waks E 2023 An atomic frequency comb memory in rare-earth-doped thin-film lithium niobate *ACS Photon.* **10** 1104
[59] Zhong T and Goldner P 2019 Emerging rare-earth doped material platforms for quantum nanophotonics *Nanophotonics* **8** 2003
[60] Mallahzadeh H 2015 Cavity-enhanced waveguide quantum memory *PhD Thesis* University of Calgary
[61] Zhong T *et al* 2017 Nanophotonic rare-earth quantum memory with optically controlled retrieval *Science* **357** 1392
[62] Zhong T, Kindem J M, Miyazono E and Faraon A 2015 Nanophotonic coherent light–matter interfaces based on rare-earth-doped crystals *Nat. Commun.* **6** 8206
[63] Zhong T, Kindem J M, Rochman J and Faraon A 2017 Interfacing broadband photonic qubits to on-chip cavity-protected rare-earth ensembles *Nat. Commun.* **8** 14107
[64] Lei M, Fukumori R, Rochman J, Zhu B, Endres M, Choi J and Faraon A 2023 Many-body cavity quantum electrodynamics with driven inhomogeneous emitters *Nature* **617** 271